nature astronomy

ARTICLES

https://doi.org/10.1038/s41550-020-01246-3

Check for updates

Detection of two bright radio bursts from magnetar SGR 1935 + 2154

F. Kirsten[1]✉, M. P. Snelders[2], M. Jenkins[2], K. Nimmo[2,3], J. van den Eijnden[2,5], J. W. T. Hessels[2,3], M. P. Gawroński[4] and J. Yang[1]

Fast radio bursts are millisecond-duration, bright radio signals (fluence 0.1–100 Jy ms) emitted from extragalactic sources of unknown physical origin. The recent CHIME/FRB and STARE2 detection of an extremely bright (fluence ~MJy ms) radio burst from the Galactic magnetar SGR 1935+2154 supports the hypothesis that (at least some) fast radio bursts are emitted by magnetars at cosmological distances. In follow-up observations totalling 522.7 h on source, we detect two bright radio bursts with fluences of 112 ± 22 Jy ms and 24 ± 5 Jy ms, respectively. Both bursts appear to be affected by interstellar scattering and we measure significant linear and circular polarization for the fainter burst. The bursts are separated in time by ~1.4 s, suggesting a non-Poissonian, clustered emission process—similar to those seen in some repeating fast radio bursts. Together with the burst reported by CHIME/FRB and STARE2, as well as a much fainter burst seen by FAST (fluence 60 mJy ms), our observations demonstrate that SGR 1935+2154 can produce bursts with apparent energies spanning roughly seven orders of magnitude, and that the burst rate is comparable across this range. This raises the question of whether these four bursts arise from similar physical processes, and whether the fast radio burst population distribution extends to very low energies (~10^{30} erg, isotropic equivalent).

Many different progenitor and emission models have been proposed to explain the fast radio burst (FRB) phenomenon[1], with one popular class of theories invoking neutron stars with exceptionally strong (10^{14}–10^{16} G) magnetic fields, commonly known as magnetars. Until now, the absence of multiwavelength detections of prompt emission[2,3] as well as the large distances to FRBs (FRB 180916.J0158+65 is the closest known, at ~150 Mpc (ref. [4])) have made it hard to study their broadband emission mechanism and local environments. This limits the avenues to differentiate between competing models. The localization of very nearby (tens of megaparsecs) FRBs could help, as would the discovery of an FRB source, at kiloparsec distances, in the Milky Way.

On 2020 April 28 a breakthrough was made when the CHIME/FRB Collaboration[5] and Bochenek et al.[6] independently detected an extremely bright radio burst from the Galactic magnetar SGR 1935+2154, using the Canadian Hydrogen Intensity Mapping Experiment Fast Radio Burst Project (CHIME/FRB[7]) and the Survey for Transient Astronomical Radio Emission 2 (STARE2[8]), respectively. The reported burst fluence was 1.5 MJy ms at 1.4 GHz (ref. [6]), and the equivalent isotropic energy of the burst was approximately three orders of magnitude greater than any previously observed magnetar radio burst. The specific energy of the burst is similar to, although approximately 30 times less than, the specific energy of the faintest known FRB[4,6]. These detections strongly suggest that at least some FRBs are produced by magnetars. For this reason, this burst has been referred to as FRB 200428 in the literature. While it is not conclusively established that this burst comes from the same physical process(es) as extragalactic FRBs, we will nonetheless use this nomenclature for the rest of this paper.

Temporally coincident with the radio pulse, a bright, hard X-ray burst was detected independently by the Konus-Wind[9], INTEGRAL[10], AGILE[11] and Insight-HXMT[12] satellites. SGR 1935+2154 has been known to undergo periods of X-ray outbursts in 2014, 2015 and 2016, but simultaneous radio observations at these times did not produce any significant detections[13]. The radio bursts from this most recent outburst are the first to be detected from this source, and the simultaneous radio/X-ray detection is a first for any Galactic magnetar (or FRB source) in general.

A few days after the announcement of FRB 200428, Zhang et al.[14] used the Five-Hundred-Meter Aperture Spherical Radio Telescope (FAST[15]) to detect a much fainter (fluence 60 mJy ms), highly linearly polarized burst from SGR 1935+2154. Its polarization properties are very similar to those of FRB 121102 (ref. [16]) and FRB 180916.J0158+65 (ref. [17]).

The detection of more radio bursts from SGR 1935+2154, and a more detailed characterization of its activity levels, can help understand whether it is genuinely an FRB source, with similar physical nature to the sources of (repeating) extragalactic FRBs. Given the great brightness of FRB 200428, a coordinated campaign of small radio telescopes (25 m diameter) with large on-sky time (hundreds of hours) can complement deeper but shorter campaigns using larger radio telescopes. Furthermore, the relatively narrow-band emission seen from some FRBs[18–20] motivates a coordinated, multitelescope campaign that spans a wide range of radio frequencies simultaneously.

Data

Between 2020 April 29 and 2020 July 27 we observed SGR 1935+2154 for a total of 763.3 h, which corresponds to 522.7 h of on-source time, taking overlap between the participating stations into account. The stations involved were the 25 m single dish RT1 at Westerbork in the Netherlands, the 25 m and 20 m telescopes at

[1]Department of Space, Earth and Environment, Chalmers University of Technology, Onsala Space Observatory, Onsala, Sweden. [2]Anton Pannekoek Institute for Astronomy, University of Amsterdam, Amsterdam, The Netherlands. [3]ASTRON, Netherlands Institute for Radio Astronomy, Dwingeloo, The Netherlands. [4]Institute of Astronomy, Faculty of Physics, Astronomy and Informatics, Nicolaus Copernicus University, Toruń, Poland. [5]Present address: Department of Physics, Astrophysics, University of Oxford, Oxford, UK. ✉e-mail: franz.kirsten@chalmers.se

Onsala Space Observatory in Sweden and the 32 m dish in Toruń, Poland (see Table 1 and Methods for details). All stations operated independently as single dishes, recording 2-bit baseband data (circular polarizations) in VLBI Data Interchange Format (VDIF)[21]. The data from all four stations were processed and searched for bursts at Onsala Space Observatory using a pipeline that was developed to search for FRBs in baseband data. In essence, the pipeline uses standard pulsar software (DSPSR[22]) in combination with Heimdall and FETCH[23] to create channelized total intensities, search for single pulses and classify the candidates as radio frequency interference (RFI) or potential real bursts (Methods).

To investigate the presence of X-ray bursts from SGR 1935+2154, we searched the HEASARC archive (https://heasarc.gsfc.nasa.gov) for X-ray observations performed simultaneously with our radio observations. We found relevant overlap with our radio campaign at the Neutron Star Interior Composition Explorer (NICER), Neil Gehrels Swift Observatory (Swift) and Fermi (see Methods for details). Finally, we considered the observing schedule (http://enghxmt.ihep.ac.cn/dqjh/317.jhtml) and burst list (http://enghxmt.ihep.ac.cn/bfy/331.jhtml)[24] from the Hard X-Ray Modulation Telescope (HXMT)[25].

Table 1 | Observational set-up

Station[a]	Band[b]	Bandwidth[c] (MHz)	SEFD[d] (Jy)	Completeness[e] (Jy ms)	Time observed[f] (h)
Wb	P	40	2,100	78	102.6
Wb	L_{Wb}	100	420	10	278.8
O8	L_{O8}	100, 175, 250	350	8, 6, 5	208.5
Tr	C	240	220	3	151.0
O6	X	500	785	8	22.4
Total telescope time/total time on source (h)[g]					763.3/522.7

[a]Wb, Westerbork RT1; O8, Onsala 25 m; Tr, Toruń; O6, Onsala 20 m. [b]P, 314–377 MHz; L_{Wb}, 1,260–1,388 MHz; L_{O8}, varying ranges between 1,227 and 1,739 MHz, see full details in Supplementary Table 1; C, 4,550–4,806 MHz; X, 8,080–8,592 MHz. [c]Effective bandwidth accounting for RFI and band edges. [d]System equivalent flux density, from the EVN status page (http://old.evlbi.org/user_guide/EVNstatus.txt). [e]Assuming a 7σ detection threshold. [f]Please see Extended Data Fig. 1 and Supplementary Table 1 for exact time ranges of the observations. [g]Total time on source accounts for overlap between the participating stations.

Results

We detected two bursts in the data from Westerbork (Wb, central observing frequency $\nu = 1{,}324.0$ MHz, Table 1) on 2020 May 24 at barycentric arrival times 22:19:19.67464 Universal Time (UT) and 22:19:21.07058 UT (B1 and B2, respectively, dispersion corrected to infinite frequency). Heimdall detected the bursts at a signal-to-noise ratio (S/N) of 81.9 for B1 and 24.6 for B2. FETCH (model A), in turn, reports a probability of 1.0 for both bursts to be of astrophysical origin.

We subsequently create coherently dedispersed filterbanks with the software correlator SFXC[26] using the dispersion measure (DM) of SGR 1935+2154 ($DM_{SGR} = 332.7206$ pc cm^{-3} (ref. [5], Methods). In Fig. 1 we show the resulting dynamic spectra and full-polarization burst profiles. A coherently dedispersed filterbank with a time resolution of 8 μs and a frequency resolution of 500 kHz is used to determine the arrival times, fluences, peak flux densities, spectral energy densities, intrinsic pulse widths, observed burst widths and scattering timescales. The dynamic spectra are summed over frequency to create a normalized time series. We fit a Lorentzian distribution to the autocorrelation function of the time series to determine the full-width at half-maximum (FWHM) of the burst profiles. The resulting observed burst widths are 866 ± 43 μs for B1 and 961 ± 48 μs for B2, and are shown using a dark-cyan bar in Fig. 1. The fluences of the bursts are determined by integrating over the light-cyan bars shown in Fig. 1, which have widths of 2 and 1.5 times the FWHM for B1 and B2, respectively. These factors were chosen such that the light-cyan bars fully cover the entire burst envelope. The fluence and peak flux density are converted to physical units using the radiometer equation[27], and the spectral energy density is determined assuming a distance to SGR 1935+2154 of $d = 9.0 \pm 2.5$ kpc (ref. [28]). The burst properties are presented in Table 2. Given the system equivalent flux density and available bandwidth at each station, we estimate our burst searches to be complete to the 7σ-fluence limits listed in Table 1.

Polarimetric properties of the bursts. We used full-polarization data, with time and frequency resolution 32 μs and 125 kHz, respectively, to study the polarimetric properties of the bursts from SGR 1935+2154. In this analysis we did not perform a calibration scan for polarimetric calibration. Instead, we used our test pulsar observation, of PSR J1935+1616, to determine the leakage correction (10%) and the delay correction (~2 ns) between the recorded right and left circular polarizations (Extended Data Fig. 2, Methods). We assume that there are no substantial changes to the calibration required between the test pulsar scan and the detected bursts, as the respective scans are less than 1 h apart.

We measure the rotation measure (RM) of B2 to be $RM_{B2} = 107 \pm 18$ rad m^{-2} (Methods), consistent with the previous measurements[5,14]. For burst B1, however, we cannot measure the RM, which we attribute to the double-component structure seen in B1 (Fig. 2). The possibly two independent bursts overlap in time such that their polarization properties are superimposed, which effectively leads to a depolarized signal. We deem the depolarization unlikely to arise from a notable change to the calibration solutions, since we find consistent results from PSR J1935+1616 (before burst B1) and burst B2 (1.4 s after B1). Assuming that the RM has not changed significantly between the two bursts, that is, the RM of burst B1 is consistent with B2, we use RM_{B2} to de-Faraday both B1 and B2. In Fig. 1 we show the Faraday-corrected (Methods) polarization profiles of both bursts, and the polarization position angle, $PPA = 0.5 \arctan(U/Q)$. For B2, the PPA is consistent with being flat across the burst profile, similar to previous reports[5]. In Table 2, we quote the linear and circular polarization fractions for B1 and B2 determined by summing the polarization profile and dividing by the sum of the Stokes I profile. The uncertainties quoted are 1σ errors, assuming that the errors in the Stokes parameters are independent, and the error in each time bin is independent. The uncertainties quoted also do not encapsulate calibration uncertainties or the effect of removing the background from the data.

Scattering and scintillation. To determine the scattering times, a Gaussian profile convolved with an exponential decay, that is, a thin-screen model for interstellar scattering, is fitted to each profile. As can be seen in the burst profiles of Fig. 1, B1 exhibits a double-peaked structure. Therefore, we fit both a single- and a double-component burst to the profile of B1. For the double-component fit, the decay time was fixed to be the same for both components. We find a reduced chi-square value $\chi_\nu^2 = 1.6$ for the single-component fit and $\chi_\nu^2 = 1.2$ for the double-component fit. Furthermore, the difference in the χ^2 value, $\Delta\chi^2$, is 136 for three additional degrees of freedom, which indicates that the double-component fit is a $>11\sigma$ improvement over the single-component fit. We conclude that B1 is consistent with exhibiting a double-component temporal structure. For B2 we find $\chi_\nu^2 = 1.0$. The double-component fit for B1 and the single-component fit for B2 result in scattering times $\tau_{B1} = 315 \pm 12$ μs and $\tau_{B2} = 299 \pm 29$ μs. The weighted average is $\bar{\tau} = 313 \pm 31$ μs at 1,324 MHz, where we added the uncertainties in quadrature. Within the model of a thin scattering screen, where the scattering timescale

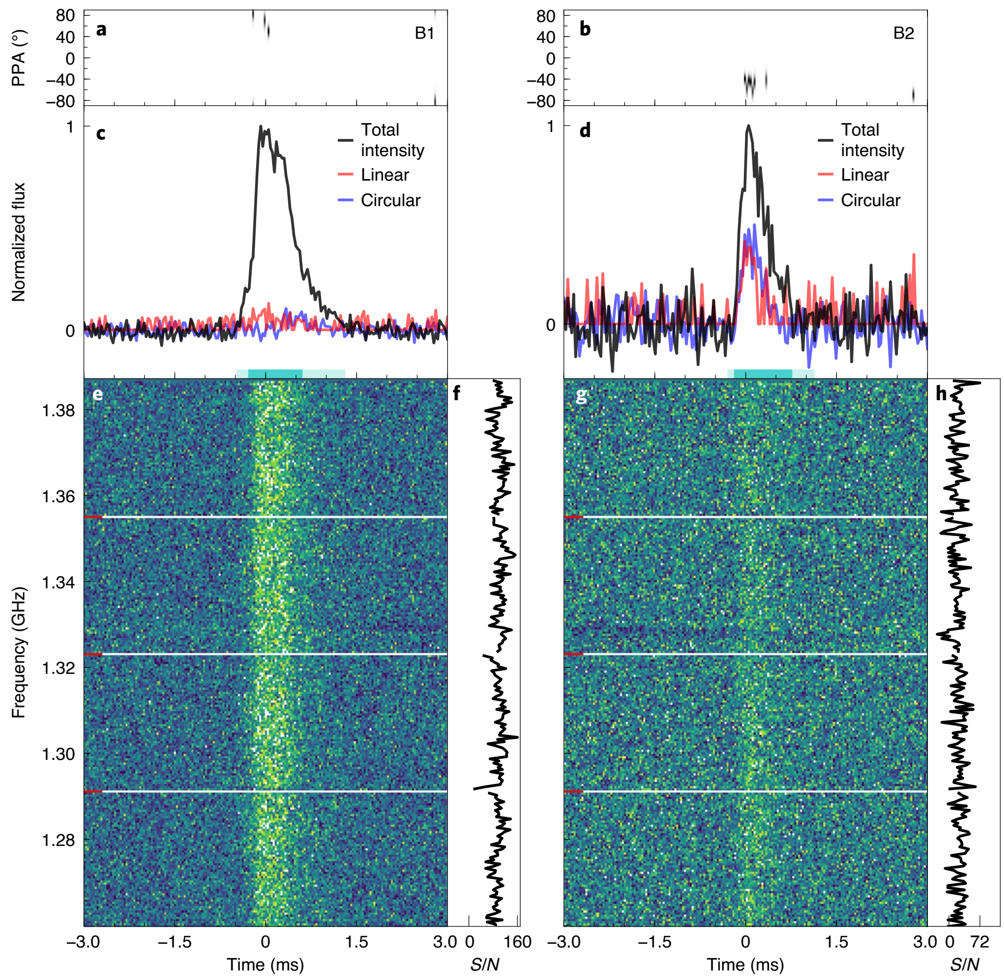

Fig. 1 | Full-polarization profiles and dynamic spectra of the two bursts. B1 and B2 are displayed in the left and right columns, respectively. The bursts are plotted with time and frequency resolutions of 32 µs and 500 kHz, respectively, and are coherently dedispersed using a DM of 332.7206 pc cm^{-3}. **a**,**b**, PPA. The greyscale represents the probability distribution of the PPA[64], the darker shading representing higher polarized *S/N*. The PPA is masked below the linear *S/N* of 3. **c**,**d**, Band-averaged profiles. The dark-cyan bars represent the FWHM (Table 2) of the burst profile as determined with a Lorentzian fit to the autocorrelation function of the bursts in the time direction. The light-cyan bars are 2 and 1.5 times the FWHM of B1 and B2, respectively. The cyan bars are placed such that they maximize the derived fluence. The total intensity burst profile is shown in black; the red and blue profiles represent the Faraday-corrected unbiased linear (equation (6)) and circular polarization, respectively. **e**,**g**, Dynamic spectra. The white bands marked with red ticks in the dynamic spectra indicate frequency channels that have been masked due to subband edges. For visual purposes the limits of the colour map have been set to the 1st and 99th percentiles of the dynamic spectrum. The dark bands in the 1.325–1.335 GHz region are due to persistent RFI. **f**,**h**, Time-scrunched, bandpass-corrected spectra computed as the sum of the dynamic spectrum under the light-cyan bars in **c** and **d**. The displayed times are referenced to the arrival times listed in Table 2.

τ and the scintillation bandwidth ν_{scint} are related via $2\pi\tau\nu_{scint} = 1$, our $\bar{\tau}$ implies a scintillation bandwidth of about 500 Hz. An autocorrelation analysis of coherently dedispersed data with a frequency resolution of 488 Hz yields no scintillation bandwidth larger than the width of one channel. Producing a filterbank with even higher frequency resolution would require a time resolution of >4 ms, and would reduce the *S/N* of any apparent scintillation because this timescale is substantially longer than the burst duration.

Burst rates. The time span between bursts B1 and B2 is only ~1.4 s, which is very short compared with the roughly 421 h total duration of non-overlapping observations taken at L-band. Therefore, we assume a Weibull distribution[29] to estimate the burst rate r and the shape parameter k valid in this frequency band (Methods). The most likely values of k and r taken jointly are $k = 0.18$ and $r = 0.11$ d^{-1} (Fig. 3). Moreover, the 68% confidence interval for k is 0.11–0.27, while the 68% confidence interval for r is 0.10–0.93 d^{-1}. Thus the data do not support a Poissonian model (for which $k = 1$), and there is evidence for clustering. Interestingly, the 95% confidence interval for k (0.08–0.42) is consistent with the 2σ region for k derived for FRB 121102 (refs. [29,30]; Fig. 3). This is an intriguing similarity between repeating extragalactic FRBs and SGR 1935+2154, although we cannot draw inferences about the exact mechanism itself.

X-ray bursts during the radio campaign. The pointed Swift and NICER observations did not reveal any X-ray bursts from SGR 1935+2154. While the source was in the field of view of Fermi/Gamma-ray Burst Monitor (GBM) during the two radio bursts on 2020 May 24, no simultaneous X-ray bursts were detected. HXMT was not observing SGR 1935+2154 during the radio bursts[24], and the source was not in the Swift/Burst Alert Telescope (BAT) field of view at that time.

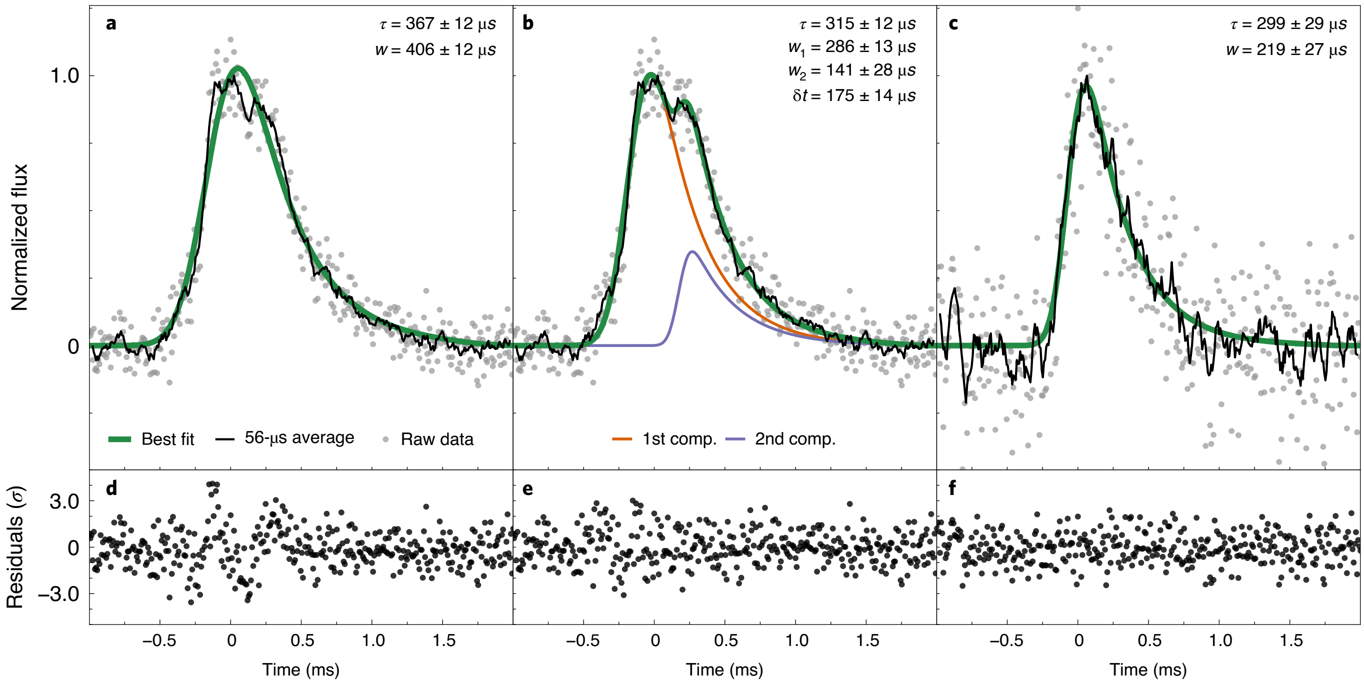

Fig. 2 | Time series of the bursts. We fit a Gaussian distribution convolved with a one-sided exponential decay to both bursts. **a**,**b**, For B1 we attempted both a single-component fit (**a**), and a two-component fit (**b**) in which we keep τ the same for both components (orange and purple lines show the individual components). **c**, Single-component fit for B2. **d**–**f**, The residuals for each fit. Grey dots display the raw data. The best fits are solid green lines and, for visual purposes, a 56 μs running average has been plotted as a solid black line. Fitting results are displayed in each panel, where τ and w denote the fitted scattering timescale and width of the Gaussian, respectively. Uncertainties denote the 1σ statistical errors of the fits. In **b** we fit separate widths, w_1 and w_2, for the components and denote the delay between the peaks of the two Gaussians as δt. It is obvious from the residuals and the quality of the fits that a two-component model provides a much better fit to B1 (see text for details).

On the other hand, several X-ray bursts were observed overlapping with our radio monitoring, without associated radio burst detections. No radio bursts[31] were seen during the X-ray burst detected with several X-ray instruments[32] on 2020 May 10. Similarly, no radio burst was observed when Fermi triggered on an SGR 1935+2154 burst on 2020 May 20 (event bn200520908). We fitted the spectrum of this burst with a double-blackbody model (BBODY+BBODY in XSPEC), adding a cross-correlation multiplication constant between the spectra from detectors n3, n6 and n7. We measure temperatures of $kT_{\rm BB,1} = 5.2 \pm 0.4$ keV and $kT_{\rm BB,2} = 16.7^{+6.7}_{-3.8}$ keV for a fit with $\chi_\nu^2 = 137.8/129 = 1.07$. We measure an 8–200 keV fluence of $(3.6 \pm 0.3) \times 10^{-7}$ erg cm^{-2}.

Comparing the HXMT burst list with the radio campaign, we find 59 X-ray bursts overlapping the radio observations (Supplementary Table 2). None of these is accompanied by a radio burst. At the time of writing, no information beyond fluence and T_{90} values is reported for these bursts[24]. The brightest of these 59 overlapping X-ray bursts had a fluence of 2.01×10^{-6} erg cm^{-2}, much brighter than the Fermi burst discussed above. The faintest of these X-ray bursts, on the other hand, had a reported fluence of 8.64×10^{-12} erg cm^{-2}.

Discussion

The rate and shape parameter determined above are valid for bursts brighter than our detection threshold of 8–10 Jy ms in the L-band (Table 1). It is possible that we have missed bursts of lower fluence, such as the one reported by Zhang et al.[14] On the other hand, the two bursts that we see within 522.7 h on source are well above our detection threshold. In combination with the first known burst[5,6], which is also the only one detected within hundreds of hours of observations with CHIME/FRB and STARE2, this is indicative of an almost flat cumulative distribution function of burst energies (Fig. 4). Assuming that a single emission mechanism is responsible for all reported radio bursts from SGR 1935+2154, it has to be of such a type that the burst rate is close to independent of the amount of energy emitted across more than seven orders of magnitude. Alternatively, different parts of the emission cone might cross our line of sight if the beaming direction changes notably over time.

We note that there also exists an upper detection threshold, which we estimate to be of the order of 10 kJy ms for our system. Any signal above this fluence could lead to nonlinearities in the receiver system causing us to miss such bursts. However, during the time range of our observations neither CHIME/FRB nor STARE2 reported further bursts as bright as FRB 200428. In addition, there is no S/N limit above which signals are masked as RFI in our analysis. Thus, it appears unlikely that we have missed any extremely bright bursts during our observations.

Polarimetry. Zhang et al.[14] presented the detection of a low-fluence, highly linearly polarized burst from SGR 1935+2154 with no circular polarization detected. This is in contrast to the polarization properties of the two bursts presented in this work. Our B2 is much less strongly polarized than the $L/I \approx 100\%$ of the FAST-detected burst, and B1 exhibits no significant polarization (<10%) at all. Radio magnetars show a wide range of polarization properties[33–35]; it is possible, perhaps unsurprising, that B1 and B2 are intrinsically not ~100% polarized. However, we find evidence for scattering in the burst profiles of both B1 and B2, which could lead to partial depolarization[34,35]. Alternatively, the low linear polarization observed in burst B1 could be caused by the superposition of the polarization properties of the two closely spaced sub-bursts (Fig. 2).

A diverse range of polarization properties are also observed for FRBs, with linear polarization fractions ranging from ~0 to 100% (refs. [16,36–38]).

Table 2 | Burst properties

	B1	B2
Barycentric arrival time (MJD)[a]	58993.93008882	58993.93010498
DM (pc cm^{-3})[b]	332.85 ± 0.21	332.94 ± 0.21
Fluence (Jy ms)[c,d]	112 ± 22	24 ± 5
Peak flux density (Jy)[c]	170 ± 34	64 ± 13
Spectral energy density (erg Hz^{-1})[c,e]	$(1.1^{+1.0}_{-0.6})\times10^{22}$	$(2.3^{+2.2}_{-1.3})\times10^{21}$
Intrinsic pulse width (μs)[f]	427 ± 33[g]	219 ± 27
Observed burst width (μs)[h]	866 ± 43	961 ± 48
Scattering timescale (μs)	315 ± 12	299 ± 29
Decorrelation bandwidth (Hz)	<500	<500
Linear polarization L_{unbias}/I (%)[i]	8.3 ± 1	27.7 ± 2
Circular polarization $\|V\|/I$ (%)[i]	7.7 ± 1	39.4 ± 3

[a]Time of arrival of the peak of the burst envelope at the Solar System barycentre after correcting to infinite frequency using DM = 332.7206 pc cm^{-3}. MJD, modified Julian date. [b]Determined using PSRCHIVE's pdmp. [c]Uncertainties are based on a 20% uncertainty in the system temperature measurements. [d]Integrated over the light-cyan bar shown in Fig. 1. [e]Assuming $d = 9.0 \pm 2.5$ kpc (ref. [28]). [f]Defined as the FWHM of the Gaussian component before convolution. [g]As per the sum of the two widths from the two-component fit in Fig. 2. [h]Defined as the FWHM of the Lorentzian distribution fitting the autocorrelation function of the time series and using a 10% fractional error. [i]Errors quoted are 1σ statistical errors, which assume that the errors on the Stokes parameters are independent, and the errors are independent per time bin. These uncertainties do not account for calibration errors and the effect of removing the baseline.

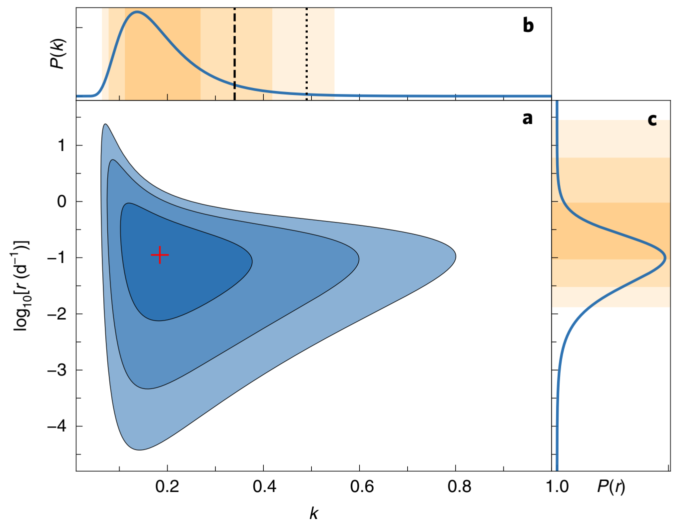

Fig. 3 | Posterior distribution of *k* and *r* parameters of the Weibull distribution. a, The full two-dimensional distribution, with the red cross corresponding to the point of maximum probability density, and the shaded blue contours representing the 68%, 95% and 99% confidence regions surrounding the maximum. **b**,**c**, The marginal distributions for *k* (**b**) and for *r* (**c**); the orange shading represents the 68%, 95% and 99% confidence intervals. The black dashed and black dotted lines indicate the best-fit values of *k* determined for FRB 121102 (refs. [29,30]). Note that the distribution of *r* looks symmetric due to the logarithmic scale, but it is actually skewed towards larger values.

Simultaneity of X-ray and radio bursts. During the CHIME/FRB and STARE2 radio burst, with an estimated fluence of 1.5 ± 0.3 MJy ms at 1,378 MHz (ref. [6]), an X-ray burst with a fluence in the range of ~6.1–9.7 × 10^{-7} erg cm^{-2} was detected by INTEGRAL, Konus-Wind and HXMT (in different energy ranges between 1 and 500 keV (refs. [9,10,12]); note that AGILE also detected the burst but has not yet reported a fluence measurement). Our brightest burst seen on 2020 May 24, B1, had a fluence four orders of magnitude weaker than the burst seen by STARE2. Assuming similar ratios[10] between radio and X-ray fluence during both bursts (~10^{-5}), we would expect a fluence of the order of 10^{-10} erg cm^{-2} in X-rays. As this value is orders of magnitude lower than typical detection thresholds for Fermi (of the order of 10^{-7} erg cm^{-2} for ~1 s bursts[39,40]), it is not surprising that Fermi detects no X-ray bursts during the radio bursts.

Conversely, another three bright X-ray bursts coincident with our campaign were reported and a further 59 overlapping bursts are listed in Supplementary Table 2. We found no radio counterparts to any of these bursts in our radio observations[31], which allows us to place upper limits on the radio fluences—as listed in Table 1. Lin et al.[41] also report a non-detection of pulsed radio emission in an observing campaign with FAST, during which 29 high-energy bursts were reported by Fermi/GBM. Therefore it seems that the majority of X-ray/gamma-ray bursts are not associated with pulsed radio emission. The parameters and fluences that we measure for the X-ray bursts are consistent with typical values observed for SGR 1935+2154 (ref. [42]), fitting with the idea that radio bursts are instead associated with atypical, harder-X-ray bursts[43].

Implications for magnetars and FRBs. To date, five Galactic magnetars, all of which are considered 'transient magnetars', have shown pulsed radio emission[44,45]. This emission is transient, lasting weeks to months, and associated with an X-ray outburst. In comparison with the radio-pulsing magnetars, SGR 1935+2154 produces much more sporadic bursts, suggesting that high-cadence monitoring of other Galactic magnetars might also discover radio bursts associated with X-ray burst storms. Along with SGR 1935+2154, the discovery of two bright, sporadic bursts from the radio-emitting magnetar J1550−5418 (ref. [46]) strengthens the idea that this may not be uncommon.

The 1.396 s separation between bursts B1 and B2 corresponds to 0.43 of SGR 1935+2154's 3.245 s rotational period. Currently it is impossible to assign rotational phases to our and all other detected radio and X-ray bursts from SGR 1935+2154 due to the lack of a phase-coherent rotational ephemeris. This is important though for understanding the burst emission mechanism. It might contribute to understanding the apparent lack of burst arrival time periodicity from repeating FRBs, which could in principle be attributed to bursts occurring at a wide and varying range of rotational phases[47], that is from varying emission sites—as opposed to being from a relatively stable location of origin, as is the case in rotation-powered radio pulsars. Our SGR 1935+2154 results suggest that its bursts can occur at a wide range of rotational phases, but with only two bursts we cannot rule out a more stable pulse–interpulse configuration.

The four reported radio bursts from SGR 1935+2154 span more than seven orders of magnitude in observed fluence. While beaming of the radio emission certainly must affect the observed fluences at some level, this nonetheless demonstrates that SGR 1935+2154's radio burst emission spans the typical luminosities seen from rotation-powered radio pulsars up to the closest known extragalactic FRBs (see Fig. 4). It is unclear whether the four known SGR 1935+2154 bursts were produced by exactly the same type of physical process. Neutron stars are known to produce radio bursts of various types (polar-cap pulsar emission, giant pulses, radio magnetar emission). Perhaps the observational differences between the bursts from repeating and (apparently) non-repeating sources are also a reflection of this diversity of emission mechanisms seen from neutron stars.

Observationally, one can pose the question: are low-luminosity radio bursts, that can only be detected from a Galactic source, also 'FRBs'? The repeater FRB 121102 has been observed to produce radio bursts with fluences spanning three orders of magnitude; for

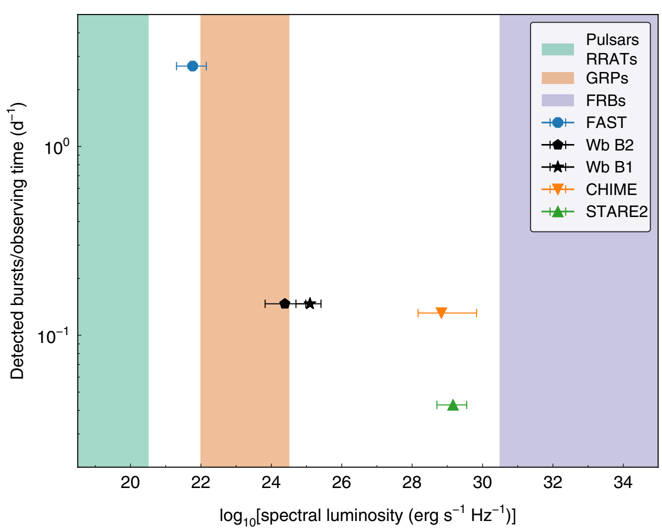

Fig. 4 | Burst occurrence per observing time and associated spectral luminosity. We display estimates for FAST[14], CHIME/FRB[5], STARE2[6] and this work. Error bars are 1σ uncertainties, which are dominated by the uncertainty of the distance[28] to SGR 1935+2154. The shaded regions indicate typical spectral luminosities for pulsars and rapidly rotating astrophysical transients (RRATs), giant radio pulses (GRPs) and FRBs[6]. It is obvious that the bursts reported for SGR 1935+2154 cannot be assigned to any of the three categories alone and that their detection rates are confined to a region spanning less than three orders of magnitude while the burst energies span close to eight orders of magnitude (Methods).

FRBs in general, the detection of lower/higher fluences is limited by telescope sensitivity and available observing time, respectively.

Overall, SGR 1935+2154 makes a compelling case that there is a link between (at least some) FRBs and magnetars. However, important observational differences remain. For instance, some repeating FRBs have shown periodicity in their activity level[48] on timescales of weeks to months—suggesting that the source may be in a binary system, extremely slowly rotating, or rapidly precessing[49–51]. SGR 1935+2154 is not known to be in a binary, and there are not yet enough detected radio bursts to look for a periodicity in its radio burst activity. Using 174 X-ray bursts detected from 2014–2020, Grossan[52] claims periodic windowed activity with a period of 232 days and a fractional activity window of 56%. Continued radio monitoring of SGR 1935+2154 may help verify this claim.

So SGR 1935+2154 is not a flawless analogue of the extragalactic FRB population. Nonetheless, magnetars can plausibly explain the diverse phenomena observed from FRBs. Perhaps the distant, periodically active FRB sources are brighter and more active because they are substantially younger than SGR 1935+2154 and because their magnetospheres are perturbed by the ionized wind of a nearby companion. Similarly, perhaps non-repeating FRBs are older, non-interacting and thus less active. Detailed characterization of FRB local environments is critical to investigating these possibilities.

Methods

Observations. *Radio observations.* Since the announcement of FRB 200428 (refs. [53,54]), we have observed SGR 1935+2154 daily for up to almost 12 h, between 2020 April 29 UT 22:45 (MJD 58968.94791) and 2020 May 25 UT 09:00 (MJD 58994.37500). After detecting bursts, we resumed the campaign with a similar cadence between 2020 June 24 UT 19:30 (MJD 59024.81250) and 2020 July 27 UT 04:30 (MJD 59057.18750). See Extended Data Fig. 1, Table 1 and Supplementary Table 1 for a summary of the observing campaign. The telescopes involved were the 25 m single dish RT1 at Westerbork in the Netherlands (Wb; P- and L-bands), the 25 m and 20 m telescopes at Onsala Space Observatory in Sweden (O8, O6; L- and X-bands) and the 32 m dish in Toruń, Poland (Tr; C-band). All stations operated independently as single dishes, recording 2-bit baseband data (circular polarizations) in VDIF[21], with the local digital baseband converters (DBBC2 or DBBC3 systems). In total, we observed for 763 h, which reduces to 522.7 h on source when accounting for overlap between the stations.

Westerbork RT1. Wb observed in two different frequency ranges, covering 313.49–377.49 MHz (P-band) split into eight 8-MHz-wide subbands during part of each run. The other part of a run covered 1,260–1,388 MHz (L-band) split at first into four 32-MHz-wide bands (29 April–19 May). This was changed to eight 16-MHz-wide bands for easier processing as of 20 May. We recorded 3 min scans with a 1 min gap in between scans during the first seven runs (29 April–06 May); for the remaining observations this was changed to 10 min recordings and 20 s gaps. At the beginning of both the P-band observations and the L-band observations we observed either pulsar PSR J1921+2153 or pulsar PSR J1935+1616 as a test source to verify the system.

Onsala. The Onsala 25 m dish (O8) observed in the L-band with varying frequency ranges and bandwidths over 14 nights. We recorded the entire available bandwidth of 512 MHz between 1,222 and 1,739 MHz during the first three observations (29 April–02 May). Owing to the large fraction of RFI (~50%) in the band we subsequently tested set-ups with 256 MHz of continuous bandwidth placed within the above range (02–09 May). Eventually, we settled for a 128-MHz-wide band split into eight 16-MHz-wide bands between 1,360 and 1,488 MHz for the rest of the campaign (Supplementary Table 1). We observed either PSR J0358+5413 or PSR J1935+1616 as a test source towards the beginning of the observations. For two runs (06–08 May) the Onsala 20 m telescope (O6) joined the observations, covering the frequency range 8,080–8,592 MHz (X-band), split into 16 32-MHz-wide subbands. Both stations O8 and O6 observed for 5–12 h during each run, recording 15 min scans with a 12 s gap in between scans.

Toruń. The 32 m dish at Toruń (Tr) observed at C-band for about 8 h during a total of 19 nights. We recorded the entire 256 MHz of bandwidth, covering the frequency range of 4,550–4,806 MHz, split into eight 32-MHz-wide subbands. We performed 5 min scans on the test pulsars at the beginning and the end of each observing run. During the first six nights (29 April–05 May) we scheduled a main 15 min observing loop that consisted of 880 s of recording on SGR 1935+2154 and 20 s gaps dedicated to gain correction. For these first runs we observed PSR J1935+1616 and PSR J2022+2854 as the test sources. Thereafter we increased the gaps by 10 s but the length of the observing loop was left unchanged. Also, from 07 May onward only PSR J2022+2854 was observed for system performance checking. We also observed during the night of 2020 May 03, for which Li et al.[55] reported a bright X-ray burst, but due to a wrong set-up the antenna was off source, hence all data were discarded.

X-ray data. Publicly available pointed observations were taken by NICER[56] and Swift[57], observing SGR 1935+2154 seven (ObsIDs 3020560107/8/25/33/37/40/42) and ten (ObsIDs 00033349049/50/56/58/60-63/66/76) times during the radio campaign, respectively. In addition, the target was in the field of view of the monitoring instruments aboard Swift (BAT) and Fermi (GBM)[58] the majority of the time. Swift/BAT did not report any burst triggers during the radio observations. Fermi/GBM records in time-tagged event (TTE) mode with a high, 2 μs, time resolution. Therefore, we focused on the Fermi/GBM data at times of particular interest in the radio campaign.

Data reduction and analysis. *Radio observations.* The baseband data from each participating station was transferred via the internet to Onsala Space Observatory, where we searched the data from each station separately with a pipeline that was developed to search for FRBs in baseband recordings. We performed the following steps on a per station basis for each recorded scan.

1. Create separate (baseband) files for each subband.
2. Channelize each subband and form Stokes *I*.
3. Splice all subbands together into one filterbank.
4. Dedisperse the filterbanks and search for bursts.
5. Classify and inspect burst candidates.
6. Create coherently dedispersed filterbanks for the best candidates and verify.

In the current recording set-up the electric voltages are sampled as 2-bit real numbers. At each station each scan (that is each integration, lasting 3–15 min, see above) is recorded in a single VDIF file that contains both polarizations of all N subbands (for example $N=8$ for Toruń, which recorded eight 32-MHz-wide subbands to capture 256 MHz of bandwidth). The software package that we use to channelize the baseband data and create total intensities (digifil from DSPSR[22]) can currently only unpack VDIF files that contain two polarizations of one single subband. Therefore, before creating 8-bit filterbanks with digifil we use jive5ab to split each scan into N separate files that contain both circular polarizations. Each subband is processed separately (but simultaneously) and the resulting filterbank files are combined into one single file that contains the entire observed frequency range with the utility splice from SIGPROC[59]. The time resolution of the filterbanks in the L-, C- and X-bands is 64 μs, while the frequency resolution is 125 kHz, 250 kHz and 2 MHz, respectively. Given $\mathrm{DM_{SGR}} = 332.7206 \pm 0.0009\,\mathrm{pc\,cm^{-3}}$ (ref. [5]), this implies a maximal intrachannel time smearing of <190 µs in our lowest channel at L-band (1,227 MHz). The filterbanks created from the P-band data have a much finer channelization (7.8 kHz) to limit residual intrachannel time smearing to ~700 µs at the lower end of the band. Time resolution is accordingly lower (1 ms) than in the other bands.

We manually inspect subsections of the data from each station to identify frequency ranges that are continuously affected by RFI. On the basis of this analysis, we create channel masks for flagging that are passed on to all subsequent steps of the burst search pipeline.

We search the filterbanks for bursts with Heimdall as the dedispersion and burst finder engine. Since the dedispersion is known a priori we do not perform a full search in DM space but instead limit the search range to $\mathrm{DM_{SGR}} \pm 50\,\mathrm{pc\,cm^{-3}}$. The candidates found by Heimdall above an S/N threshold of seven are then classified either as RFI or potential candidates by FETCH (model A)[23]. We chose this particular S/N threshold since while testing the pipeline a lower threshold led to an extensive number of false positives. This is easily explained by the fact that FETCH was trained and tested on data with $S/N \geq 8$, that is, the classifier employed by FETCH is potentially less reliable for low-S/N candidates. We inspect the candidates by eye and, as a final step, we use SFXC[26] to create coherently dedispersed filterbanks around the times of the most convincing candidates, for final verification.

As mentioned above, we observed well known pulsars in each observing run to verify the integrity of our data and the reliability of our processing pipeline. To this end, we perform the steps described above also on the pulsar scans. In addition, we fold the filterbank files that contain a scan of a pulsar with DSPSR's dspsr and inspect the folded profiles. The respective pulsars were detected each time, with the exception of PSR J1921+2153 observed with station Wb at L-band. At this frequency the pulsar was detected only about half the time, which we attribute to diffractive scintillation from the Galactic interstellar medium. The test pulsar PSR J1935+1616 is bright enough to detect several individual pulses with our pipeline almost each time it is observed.

DM optimization. To optimize the DM we run the PSRCHIVE[60] tool pdmp on the filterbank data of each burst separately, which yields $\mathrm{DM_{B1}} = 332.85 \pm 0.21\,\mathrm{pc\,cm^{-3}}$ and $\mathrm{DM_{B2}} = 332.94 \pm 0.21\,\mathrm{pc\,cm^{-3}}$ for B1 and B2, respectively. These values are consistent with $\mathrm{DM_{SGR}}$ as measured by the CHIME/FRB Collaboration[5] ($\mathrm{DM_{SGR}} = 332.7206 \pm 0.0009\,\mathrm{pc\,cm^{-3}}$), albeit marginally higher. We attribute the higher DM to the optimization algorithm employed by pdmp which essentially maximizes the S/N of the burst by modifying the DM. Given the scattering tails of the bursts, this can lead to a peak in S/N at a DM higher than the true value. We do not attempt to determine an optimal DM based on higher-time-resolution baseband data because the burst width is dominated by scattering. Furthermore, we consider $\mathrm{DM_{SGR}}$ to probably be more accurate, because of the larger fractional bandwidth of those observations.

Burst statistics. If a stochastic process can be described as a Poisson point process with a constant r, then the random variable describing the wait times δ between events generated by the process will follow an exponential distribution,

$$f(\delta|r) = r\mathrm{e}^{-r\delta} \tag{1}$$

In contrast, repeating FRBs are known to show clustering in their burst patterns, and therefore cannot be described with a Poissonian model. As described by Oppermann et al.[29], a possible generalization of the wait time distribution is given by the Weibull distribution,

$$f(\delta|k, r) = \frac{k}{\delta}\left(\delta r\,\Gamma(1 + k^{-1})\right)^k \mathrm{e}^{-(\delta r \Gamma(1+k^{-1}))^k} \tag{2}$$

which reduces to an exponential distribution if $k = 1$. Here Γ is the Gamma function. The posterior distribution of k and r can therefore be used to test whether the data support a Poissonian model, because Poissonian data should necessarily produce a posterior distribution consistent with $k = 1$. To calculate the posterior distribution, we follow the formalism described by Oppermann et al.[29] We only include scans from Westerbork and Onsala at L-band. Whenever Westerbork and Onsala overlap we only include scans taken with the Westerbork station to avoid possible correlations between scans (amounting to a grand total of 421.2 h of on-source time). Therefore, we assume that all scans are independent, and calculate the total likelihood of the data as the product of the likelihoods of each individual scan. For the scan containing B1 and B2, we use the topocentric arrival time from the beginning of the scan to calculate the likelihood function. Finally, we use a uniform prior distribution and calculate the posterior distribution in the usual way as

$$\mathrm{post}\,(k, r|\mathcal{D}) \propto L(\mathcal{D}|k, r) f(k, r) \tag{3}$$

where $L(\mathcal{D}|k, r)$ represents the likelihood of all the data, and $f(k, r)$ represents the prior.

Burst energy distribution. To create Fig. 4, we made the following simplifying assumptions. First, we considered only the active phase of SGR 1935+2154 in April and May 2020 to estimate observing hours. During this period, for CHIME/FRB and STARE2 we assumed daily exposures of 3 h and 9.2 h, respectively, for 61 days. FAST reported one burst in 9 h of observing time[14,41]. For our campaign, we considered only our non-overlapping L-band observations in April and May 2020 (163.5 h). Due to the lack of reported observed burst widths, we assume a width of 1.0 ± 0.2 ms for the bursts reported by CHIME/FRB, STARE2 and FAST. For bursts B1 and B2 we use the values listed in Table 2. Furthermore, we use the fluences as reported in the respective publications and from Table 2.

Polarimetric calibration. In our observations, we did not perform a noise-diode scan to use for polarimetric calibration. Instead, we used our test pulsar observation, PSR J1935+1616, to determine the leakage correction between the recorded right and left circular polarizations. First we assume that the leakage calibration only affects Stokes V (defined as $V = \mathrm{LL} - \mathrm{RR}$, using the PSR/IEEE convention for the Stokes parameters; RR and LL are the detected powers in right and left circular polarizations, respectively[61]). This is approximately equivalent to moving 20% of the flux density in LL to RR; that is, we correct for a 10% leakage between right and left circular polarizations. Since Wb has an equatorial mount, we do not need to apply any corrections for parallactic angle.

We still have to account for a delay between the two polarization hands, which we assume only affects Stokes Q and U. We use the tool rmfit from PSRCHIVE, which performs a search for the RM by maximizing the linear polarization fraction. Since we did not correct for the delay between the two polarization hands beforehand, this manifests as an offset in the RM (compared with the true RM of the source), assuming that the delay is constant across all frequencies. For PSR J1935+1616, we measure an RM of $+77.8\,\mathrm{rad\,m^{-2}}$, which is ~88 units from the true RM of $-10.2\,\mathrm{rad\,m^{-2}}$ (ref. [62]). Under our assumption that a delay approximately corresponds to an offset in RM, an offset of $88\,\mathrm{rad\,m^{-2}}$ translates to ~2 ns in delay. By correcting for Faraday rotation in PSR J1935+1616 using the rmfit-determined RM ($+77.8\,\mathrm{rad\,m^{-2}}$), we reproduced the polarimetric profile and PPA swing of PSR J1935+1616 within 4% of the published polarization properties[63]. Extended Data Fig. 2 shows the Faraday-corrected polarization profile and PPA swing of PSR J1935+1616 using the true RM of the source and the rmfit-determined RM, and comparing both with the profile and PPA presented in the literature[63].

We apply the 10% leakage calibration to the bursts detected from SGR 1935+2154. We first run rmfit to find the RM that maximizes the linear polarization. For burst B2, we find the rmfit-measured RM to be ~$82\,\mathrm{rad\,m^{-2}}$ higher than what was expected from the previously measured RM from an SGR 1935+2154 radio burst ($112.3\,\mathrm{rad\,m^{-2}}$; ref. [14]), which is consistent with our RM offset measured for PSR J1935+1616.

We then perform a joint QU fit to Stokes parameters Q/I and U/I as a function of ν using the following equations:

$$Q/I = L\cos[2(c^2\,\mathrm{RM}/\nu^2 + \nu\pi D + \phi)] \tag{4}$$

$$U/I = L\sin[2(c^2\,\mathrm{RM}/\nu^2 + \nu\pi D + \phi)] \tag{5}$$

where c is the speed of light, and we fit for the linear polarization fraction L, the delay between the hands D and $\phi = \phi_\infty + \phi_{\mathrm{inst}}$, where ϕ_∞ is the absolute angle of the polarization on the sky (referenced to infinite frequency) and ϕ_{inst} is the phase difference between the polarization hands. We perform the joint fit on Q/I and U/I spectra for PSR J1935+1616 and for burst B2 from SGR 1935+2154, where the delay is assumed to be the same for both the pulsar scan and the target scan. We fix the RM of the pulsar at the known[62] RM of PSR J1935+1616, $-10.2\,\mathrm{rad\,m^{-2}}$. We find $D \approx 2.5$ ns, consistent with our prediction. Additionally, we measure the RM of B2 to be $107 \pm 18\,\mathrm{rad\,m^{-2}}$, consistent with the previously measured[14] value ($112.3\,\mathrm{rad\,m^{-2}}$). The fractional error on the measured RM is large since we did not perform an independent, noise-diode polarization calibration scan, and therefore cannot remove the covariance between the fit parameters.

We debias the linear polarization fraction following Everett and Weisberg[64]:

$$L_{\mathrm{unbias}} = \begin{cases} \sigma_I\sqrt{\left(\frac{L_{\mathrm{meas}}}{\sigma_I}\right)^2 - 1} & \text{if } \frac{L_{\mathrm{meas}}}{\sigma_I} \geq 1.57 \\ 0 & \text{otherwise} \end{cases} \tag{6}$$

where $L_{\mathrm{meas}} = \sqrt{Q^2 + U^2}$, for Stokes parameters Q and U, and σ_I is the s.d. in the off-pulse Stokes I.

X-ray observations. To search for X-ray bursts during the two NICER and nine Swift/X-ray Telescope (XRT) pointed observations, we followed standard data reduction procedures in HEASOFT v6.25 to extract light curves, using the latest calibration files via the online database caldb (https://heasarc.gsfc.nasa.gov/docs/heasarc/caldb/caldb_intro.html). The NICER data were reduced using nicerdas, applying standard filtering with additional constraints (SUN_ANGLE > 60° and COR_SAX > 4) generated with nimaketime and applied with niextract-events. For Swift/XRT, we applied xrtpipeline v0.13.4. After data calibration, we extracted light curves for both observatories using xselect v2.4e at various time resolutions: 0.004, 0.1 and 1 s for NICER, 0.1 and 1 s for Swift/XRT in window-timing mode and 2.6 s for Swift/XRT in photon-counting mode. Finally, we checked our methods by following the same procedures for NICER observation 3020560101, which did not overlap with the radio campaign but was reported to contain numerous X-ray bursts[43]. We clearly recover the X-ray bursts reported therein, confirming our data reduction procedure.

For Fermi/GBM, we focused primarily on two events: first, the GBM trigger on an X-ray burst of SGR 1935+2154 on 2020 May 20, 21:47:07.548 UT (event bn200520908), and second the TTE data on 2020 May 24 22:00–23:00 UT, during which we observed radio bursts. For the GBM trigger data, we analysed the cspec files of detectors n3, n6 and n7, which showed the strongest bursts in the quicklook images. Using gspec v0.9.1, we extracted burst and background spectra per detector for the SGR 1935+2154 burst, which we then fitted jointly using xspec v12.10.1. To analyse the TTE data on 2020 May 24, we used the gtbin tool in the FERMITOOLS package to extract light curves at 0.1, 0.25 and 0.004 s time resolutions for all 12 GBM detectors. We then used the fermi gbm data tools v1.0.2, combined with the spacecraft pointing, to measure the viewing angle between each GBM detector and SGR 1935+2154. This comparison confirms that the source was visible during the radio bursts and reveals that detectors n9 and na had the smallest viewing angles, at ~41° and ~5.5°, respectively.

While Fermi/GBM triggered several additional times after the start of our radio campaign, none of these events overlapped with it: trigger bn200503976 on 2020 May 03, also reported by Ursi et al.[65] and Li et al.[55], fell into a recording gap at Wb, while station O8 was affected by exceptionally strong RFI and the Tr antenna was off source. On 2020 May 10, Fermi passed through the South Atlantic Anomaly during the X-ray burst reported by Hurley et al.[32] and no TTE data were recorded. Later on May 10, Fermi/GBM trigger bn200510911 occurred just before the start of our radio observations.

Scattering timescale and scintillation. The CHIME/FRB Collaboration[5] reports a scattering time $\tau_{\rm CHIME} = 759 \pm 8\,\mu$s at a frequency of 600 MHz, while Bochenek et al.[6] report a scattering time $\tau_{\rm STARE2} = 400 \pm 100\,\mu$s at 1 GHz. Assuming a thin-screen model for scattering and Kolmogorov turbulence, the scattering time scales with frequency as $\tau \propto \nu^{\alpha}$, with $\alpha = -4$ being the frequency scaling parameter. In this scheme, given the CHIME and STARE2 results we would expect $30\,\mu{\rm s} \lesssim \tau \lesssim 120\,\mu$s at $\nu = 1.324$ GHz. However, the value we measure is a factor $\gtrsim 2.5$ higher ($\bar{\tau} = 313 \pm 31\,\mu$s) and implies $\alpha = -1.15$, much shallower than the canonical value. We note that the scalings implied by $\tau_{\rm CHIME}$ and $\tau_{\rm STARE2}$ are very similar, with $\alpha = -1.25$. Such a shallow scaling, and the fact that Bochenek et al.[6] can reconcile their observations with no scattering, suggest that the tails we observe could be intrinsic. Along the line of sight to SGR 1935+2154, the two available electron density models, NE2001 (ref. [66]) and YMW16 (ref. [67]), predict scattering timescales of 10 μs and 1 ms, respectively; that is, in combination they support both notions of an intrinsic tail and of a scattering tail.

A number of recent studies of pulsar scattering at low radio frequencies ($\nu < 300$ MHz) also measure values for α that are lower than the theoretically expected one[68–70]. This can be caused by several factors, among which are that the assumptions of Kolmogorov turbulence and a single thin-scattering-screen geometry are in fact not valid. To measure the scattering timescale we assumed an intrinsic Gaussian pulse shape whose rise time can mimic that expected for an impulsive signal that travels through an extended screen, that is, a thick-screen geometry[71]. Moreover, the assumption of a single screen might be invalid, as SGR 1935+2154 is associated with the supernova remnant G57.2+0.8 with high probability[72]. Thus, besides an interstellar scattering screen about half way towards the source there could well be a second screen within the supernova remnant, that is much closer to the magnetar itself. In fact, Simard and Ravi[73] invoke the existence of such a screen to explain the spectral structure of the burst reported by the CHIME/FRB Collaboration[5]. In their model, the screen closest to the magnetar causes what can be interpreted as scintillation with a characteristic scintillation bandwidth of $\Delta\nu_{600} = 100$ MHz at an observing frequency of 600 MHz. Scaled to our observing frequency this translates to $\Delta\nu_{1,300} = 2,200$ MHz. This is consistent with our observations in the sense that we observe during a phase of a bright scintillation event (caused by the screen close to the source). Any scintillation that could be caused by the interstellar screen (that is also the cause for the temporal broadening) is too narrow in bandwidth for us to resolve.

Data availability

The data that support the plots within this paper and other findings of this study are available from https://doi.org/10.5281/zenodo.4044453 or from the corresponding author upon reasonable request.

Code availability

The pipeline written to process the baseband data can be found at https://github.com/pharaofranz/frb-baseband, while the code used to calculate the posterior distribution and generate Fig. 3 can be found at https://github.com/MJastro95. jive5ab can be retrieved from https://github.com/jive-vlbi/jive5ab, Heimdall is hosted at https://sourceforge.net/projects/heimdall-astro/ and FETCH can be found at https://github.com/devanshkv/fetch. The pulsar package DSPSR is hosted at https://sourceforge.net/projects/dspsr/, while SIGPROC was retrieved from https://github.com/SixByNine/sigproc.

Received: 9 July 2020; Accepted: 29 September 2020;
Published online: 16 November 2020

References

1. Platts, E. et al. A living theory catalogue for fast radio bursts. *Phys. Rep.* **821**, 1–27 (2019).
2. Chen, G., Ravi, V. & Lu, W. The multiwavelength counterparts of fast radio bursts. *Astrophys. J.* **897**, 146 (2020).
3. Scholz, P. et al. Simultaneous X-ray, gamma-ray, and radio observations of the repeating fast radio burst FRB 121102. *Astrophys. J.* **846**, 80 (2017).
4. Marcote, B. et al. A repeating fast radio burst source localized to a nearby spiral galaxy. *Nature* **577**, 190–194 (2020).
5. CHIME/FRB Collaboration A bright millisecond-duration radio burst from a Galactic magnetar. Preprint at https://arxiv.org/abs/2005.10324 (2020).
6. Bochenek, C. D. et al. A fast radio burst associated with a Galactic magnetar. Preprint at https://arxiv.org/abs/2005.10828 (2020).
7. CHIME/FRB Collaborationet al. The CHIME Fast Radio Burst Project: system overview. *Astrophys. J.* **863**, 48 (2018).
8. Bochenek, C. D. et al. STARE2: detecting fast radio bursts in the Milky Way. *Publ. Astron. Soc. Pac.* **132**, 034202 (2020).
9. Ridnaia, A. et al. A peculiar hard X-ray counterpart of a Galactic fast radio burst. Preprint at https://arxiv.org/abs/2005.11178 (2020).
10. Mereghetti, S. et al. INTEGRAL discovery of a burst with associated radio emission from the magnetar SGR 1935+2154. *Astrophys. J. Lett.* **898**, L29 (2020).
11. Tavani, M. et al. AGILE detection of a hard X-ray burst in temporal coincidence with a radio burst from SGR 1935+2154. *Astronomer's Telegram* 13686 (2020).
12. Li, C.K. et al. Identification of a non-thermal X-ray burst with the Galactic magnetar SGR 1935+2154 and a fast radio burst with Insight-HXMT. Preprint at https://arxiv.org/abs/2005.11071 (2020).
13. Younes, G. et al. X-ray and radio observations of the magnetar SGR J1935+2154 during its 2014, 2015, and 2016 outbursts. *Astrophys. J.* **847**, 85 (2017).
14. Zhang, C. F. et al. A highly polarised radio burst detected from SGR 1935+2154 by FAST. *Astronomer's Telegram* 13699 (2020).
15. Nan, R. et al. The Five-Hundred Aperture Spherical Radio Telescope (FAST) Project. *Int. J. Mod. Phys. D* **20**, 989–1024 (2011).
16. Michilli, D. et al. An extreme magneto-ionic environment associated with the fast radio burst source FRB 121102. *Nature* **553**, 182–185 (2018).
17. CHIME/FRB Collaboration CHIME/FRB discovery of eight new repeating fast radio burst sources. *Astrophys. J. Lett.* **885**, L24 (2019).
18. Hessels, J. W. T. et al. FRB 121102 bursts show complex time–frequency structure. *Astrophys. J. Lett.* **876**, L23 (2019).
19. Gourdji, K. et al. A sample of low-energy bursts from FRB 121102. *Astrophys. J. Lett.* **877**, L19 (2019).
20. Majid, W. A. et al. A dual-band radio observation of FRB 121102 with the Deep Space Network and the detection of multiple bursts. *Astrophys. J. Lett.* **897**, L4 (2020).
21. Whitney, A., Kettenis, M., Phillips, C. & Sekido, M. VLBI Data Interchange Format (VDIF). In *International VLBI Service for Geodesy and Astronomy: 2010 General Meeting Proceedings* (eds Behrend, D. & Baver, K. D.) 192–196 (NASA, 2010).
22. van Straten, W. & Bailes, M. DSPSR: digital signal processing software for pulsar astronomy. *Publ. Astron. Soc. Aust.* **28**, 1–14 (2011).
23. Agarwal, D., Aggarwal, K., Burke-Spolaor, S., Lorimer, D.R. & Garver-Daniels, N. FETCH: a deep-learning based classifier for fast transient classification. *Mon. Not. R. Astron. Soc.* **497**, 1661–1674 (2020).
24. Li, C. K. et al. Updated catalog of X-ray bursts of SGR J1935.2154 from Insight-HXMT observations. *GRB Coordinates Network* 28027 (2020).
25. Zhang, S.-N. et al. Overview to the Hard X-ray Modulation Telescope (Insight-HXMT) satellite. *Sci. China Phys. Mech. Astron.* **63**, 249502 (2020).
26. Keimpema, A. et al. The SFXC software correlator for very long baseline interferometry: algorithms and implementation. *Exp. Astron.* **39**, 259–279 (2015).
27. Cordes, J. M. & McLaughlin, M. A. Searches for fast radio transients. *Astrophys. J.* **596**, 1142–1154 (2003).
28. Zhong, S.Q., Dai, Z.G., Zhang, H.M. & Deng, C.M. On the distance of SGR 1935+2154 associated with FRB 200428 and hosted in SNR G57.2+0.8. *Astrophys. J. Lett.* **898**, L5 (2020).
29. Oppermann, N., Yu, H.-R. & Pen, U.-L. On the non-Poissonian repetition pattern of FRB121102. *Mon. Not. R. Astron. Soc.* **475**, 5109–5115 (2018).
30. Oppermann, N. et al. Repeating fast radio bursts with WSRT/Apertif. *Astron. Astrophys.* **635**, A61 (2020).

31. Kirsten, F. et al. Simultaneous multi-frequency limits on radio emission at the time of a bright X-ray burst from SGR 1935+2154. *Astronomer's Telegram* 13735 (2020).
32. Hurley, K. et al. IPN triangulation of a bright burst from SGR 1935+2154 on 2020-05-10 at 06:12 UT. *GRB Coordinates Network* 27714 (2020).
33. Kramer, M., Stappers, B. W., Jessner, A., Lyne, A. G. & Jordan, C. A. Polarized radio emission from a magnetar. *Mon. Not. R. Astron. Soc.* **377**, 107–119 (2007).
34. Camilo, F., Reynolds, J., Johnston, S., Halpern, J. P. & Ransom, S. M. The magnetar 1E 1547.0−5408: radio spectrum, polarimetry, and timing. *Astrophys. J.* **679**, 681–686 (2008).
35. Levin, L. et al. Radio emission evolution, polarimetry and multifrequency single pulse analysis of the radio magnetar PSR J1622−4950. *Mon. Not. R. Astron. Soc.* **422**, 2489–2500 (2012).
36. Petroff, E. et al. A real-time fast radio burst: polarization detection and multiwavelength follow-up. *Mon. Not. R. Astron. Soc.* **447**, 246–255 (2015).
37. Masui, K. et al. Dense magnetized plasma associated with a fast radio burst. *Nature* **528**, 523–525 (2015).
38. Ravi, V. et al. The magnetic field and turbulence of the cosmic web measured using a brilliant fast radio burst. *Science* **354**, 1249–1252 (2016).
39. Wood, J., Fermi-GBM Team & GBM-LIGO/Virgo Group. LIGO/Virgo S190930t: upper limits from Fermi-GBM observations. *GRB Coordinates Network* 25887 (2019).
40. Wood, J. & Fermi-GBM Team. Fermi-LAT ANTARES coincidence: upper limits from Fermi-GBM observations. *GRB Coordinates Network* 26676 (2020).
41. Lin, L. et al. Stringent upper limits on pulsed radio emission during an active bursting phase of the Galactic magnetar SGRJ1935+2154. Preprint at https://arxiv.org/abs/2005.11479 (2020).
42. Lin, L. et al. Burst properties of the most recurring transient magnetar SGR J1935+2154. *Astrophys. J.* **893**, 156 (2020).
43. Younes, G. et al. A possible polar origin for the FRB associated with a Galactic magnetar. Preprint at https://arxiv.org/abs/2006.11358 (2020).
44. Kaspi, V. M. & Beloborodov, A. M. Magnetars. *Annu. Rev. Astron. Astrophys.* **55**, 261–301 (2017).
45. Lower, M. E., Shannon, R. M., Johnston, S. & Bailes, M. Spectropolarimetric properties of Swift J1818.0−1607: a 1.4 s radio magnetar. *Astrophys. J. Lett.* **896**, L37 (2020).
46. Burgay, M. et al. Search for FRB and FRB-like single pulses in Parkes magnetar data. In *Pulsar Astrophysics: The Next Fifty Years* (eds Weltevrede, P. et al.) 319–321 (IAU, 2018).
47. Spitler, L. G. et al. A repeating fast radio burst. *Nature* **531**, 202–205 (2016).
48. CHIME/FRB Collaboration. Periodic activity from a fast radio burst source. *Nature* **582**, 351–355 (2020).
49. Lyutikov, M., Barkov, M. V. & Giannios, D. FRB periodicity: mild pulsars in tight O/B-star binaries. *Astrophys. J. Lett.* **893**, L39 (2020).
50. Beniamini, P., Wadiasingh, Z. & Metzger, B. D. Periodicity in recurrent fast radio bursts and the origin of ultralong period magnetars. *Mon. Not. R. Astron. Soc.* **496**, 3390–3401 (2020).
51. Levin, Y., Beloborodov, A. M. & Bransgrove, A. Precessing flaring magnetar as a source of repeating FRB 180916.J0158+65. *Astrophys. J. Lett.* **895**, L30 (2020).
52. Grossan, B. Periodic windowed behavior in SGR1935+2154 SGR bursts. Preprint at https://arxiv.org/abs/2006.16480 (2020).
53. Scholz, P. & CHIME/FRB Collaboration. A bright millisecond-timescale radio burst from the direction of the Galactic magnetar SGR 1935+2154. *Astronomer's Telegram* 13681 (2020).
54. Bochenek, C. et al. Independent detection of the radio burst reported in ATel #13681 with STARE2. *Astronomer's Telegram* 13684 (2020).
55. Li, X. B. et al. Insight-HXMT detection of a short bright burst from SGR 1935+2154. *GRB Coordinates Network* 27688 (2020).
56. Gendreau, K. C. et al. The Neutron star Interior Composition Explorer (NICER): design and development. *Proc. SPIE* **9905**, 99051H (2016).
57. Gehrels, N. et al. The Swift Gamma-Ray Burst Mission. *Astrophys. J.* **611**, 1005–1020 (2004).
58. Meegan, C. et al. The Fermi Gamma-ray Burst Monitor. *Astrophys. J.* **702**, 791–804 (2009).
59. Lorimer, D. R. SIGPROC: pulsar signal processing programs. *Astrophysics Source Code Library* ascl:1107.016 (2011).
60. van Straten, W. et al. PSRCHIVE: development library for the analysis of pulsar astronomical data. *Astrophysics Source Code Library* ascl:1105.014 (2011).
61. van Straten, W., Manchester, R. N., Johnston, S. & Reynolds, J. E. PSRCHIVE and PSRFITS: definition of the Stokes parameters and instrumental basis conventions. *Publ. Astron. Soc. Aust.* **27**, 104–119 (2010).
62. Han, J. L., Manchester, R. N., van Straten, W. & Demorest, P. Pulsar rotation measures and large-scale magnetic field reversals in the Galactic disk. *Astrophys. J. Suppl. Ser.* **234**, 11 (2018).
63. Johnston, S. & Kerr, M. Polarimetry of 600 pulsars from observations at 1.4 GHz with the Parkes radio telescope. *Mon. Not. R. Astron. Soc.* **474**, 4629–4636 (2018).
64. Everett, J. E. & Weisberg, J. M. Emission beam geometry of selected pulsars derived from average pulse polarization data. *Astrophys. J.* **553**, 341–357 (2001).
65. Ursi, A. et al. AGILE detection of a short and hard X-ray burst possibly related to SGR 1935+2154. *GRB Coordinates Network* 27687 (2020).
66. Cordes, J. M. & Lazio, T. J. W. NE2001.I. A new model for the Galactic distribution of free electrons and its fluctuations. Preprint at https://arxiv.org/abs/astro-ph/0207156 (2002).
67. Yao, J. M., Manchester, R. N. & Wang, N. A new electron-density model for estimation of pulsar and FRB distances. *Astrophys. J.* **835**, 29 (2017).
68. Kirsten, F. et al. Probing pulsar scattering between 120 and 280 MHz with the MWA. *Astrophys. J.* **874**, 179 (2019).
69. Geyer, M. et al. Scattering analysis of LOFAR pulsar observations. *Mon. Not. R. Astron. Soc.* **470**, 2659–2679 (2017).
70. Meyers, B. W. et al. Spectral flattening at low frequencies in Crab giant pulses. *Astrophys. J.* **851**, 20 (2017).
71. Williamson, I. P. Pulse broadening due to multiple scattering in the interstellar medium. *Mon. Not. R. Astron. Soc.* **157**, 55 (1972).
72. Gaensler, B. M. GRB 140705A/SGR 1935+2154: probable association with supernova remnant G57.2+0.8. *GRB Coordinates Network* 16533 (2014).
73. Simard, D. & Ravi, V. Scintillation can explain the spectral structure of the bright radio burst from SGR 1935+2154. *Astrophys. J. Lett.* **899**, L21 (2020).
74. Verrecchia, F. et al. AGILE detection of a burst from SGR 1935+2154 on May 10, 2020. *GRB Coordinates Network* 27727 (2020).

Acknowledgements

We thank R. Blaauw and P. van Dijk for scheduling and running the observations at Westerbork. At Onsala we acknowledge the help of E. Varenius with running the observations at X-band on the Onsala 20 m telescope and we thank M. Mickaliger for helping with the initial set-up for running FETCH. We appreciate the help of N. Degenaar with interpreting the X-ray observations and we are indebted to A. Keimpema, who modified SFXC to our needs. We also thank G. Younes for useful discussions; and we thank S. Kulkarni, V. Ravi, W. Majid, J. Katz, A. Tohuvavohu and B. Grossan for helpful comments. F.K. acknowledges support by the Swedish Research Council. J.v.d.E. is supported by the Netherlands Organisation for Scientific Research (NWO). Research at the University of Amsterdam and ASTRON is supported by an NWO Vici grant to J.W.T.H. This work is based in part on observations carried out using the 32 m radio telescope operated by the Institute of Astronomy of the Nicolaus Copernicus University in Toruń (Poland) and supported by a Polish Ministry of Science and Higher Education SpUB grant.

Author contributions

F.K. wrote and ran the search pipeline, led the observations at Onsala, interpreted the data and led the paper writing. M.P.S. ran the scattering analysis, created Figs. 1–4 and Extended Data Fig. 1, and populated Supplementary Table 1. M.J. performed the Weibull analysis and wrote the associated sections. M.P.S. and M.J. co-led the Westerbork observing campaign. K.N. ran the polarization analysis, created Extended Data Fig. 2, and wrote the respective sections. J.v.d.E. searched and analysed the X-ray observations, wrote the respective sections and populated Supplementary Table 2. J.W.T.H interpreted the data scientifically, supervised student work and wrote parts of the manuscript. M.P.G. led the observations at Toruń and wrote the section describing those data. J.Y. supported the observations at Onsala and also interpreted the data.

Competing interests

The authors declare no competing interests.

Additional information

Extended data is available for this paper at https://doi.org/10.1038/s41550-020-01246-3.

Supplementary information is available for this paper at https://doi.org/10.1038/s41550-020-01246-3.

Correspondence and requests for materials should be addressed to F.K.

Peer review information *Nature Astronomy* thanks George Younes and the other, anonymous, reviewer(s) for their contribution to the peer review of this work.

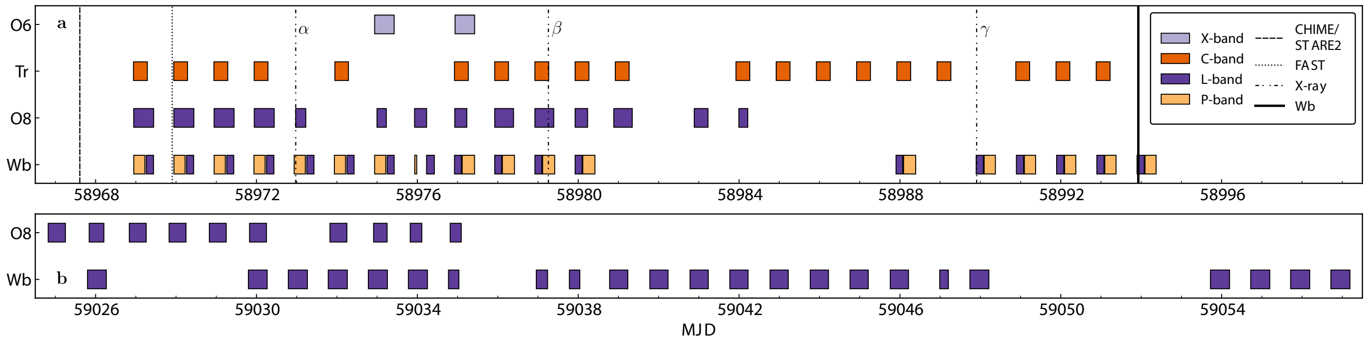

Extended Data Fig. 1 | Overview of the observations of SGR 1935+2154 during this campaign. Panels (**a**) and (**b**) both span 33 days, with observations colourcoded by observing frequency. Note the gap of 25 days between (**a**) and (**b**). No observations were conducted during that time period. Vertical lines indicate the times of reported bursts. Solid line: events found in our campaign; long-dashed: CHIME and STARE2 detections[53,54]; dotted: detection by FAST[14]; dash-dotted: X-ray bursts as reported by α) Ursi et al.[65], β) Hurley et al.[32] and Verrecchia et al.[74], γ) a Fermi/GBM trigger on 2020 May 20 at 21:47:07.548 UT. During X-ray events β) and γ) no radio counterparts were found in any of our data, which allows us to place upper limits on the fluences — as listed in Table 1. Unfortunately we can draw no conclusions from our data coincident with event α) because Wb was in a recording gap and O8 was affected by strong RFI.

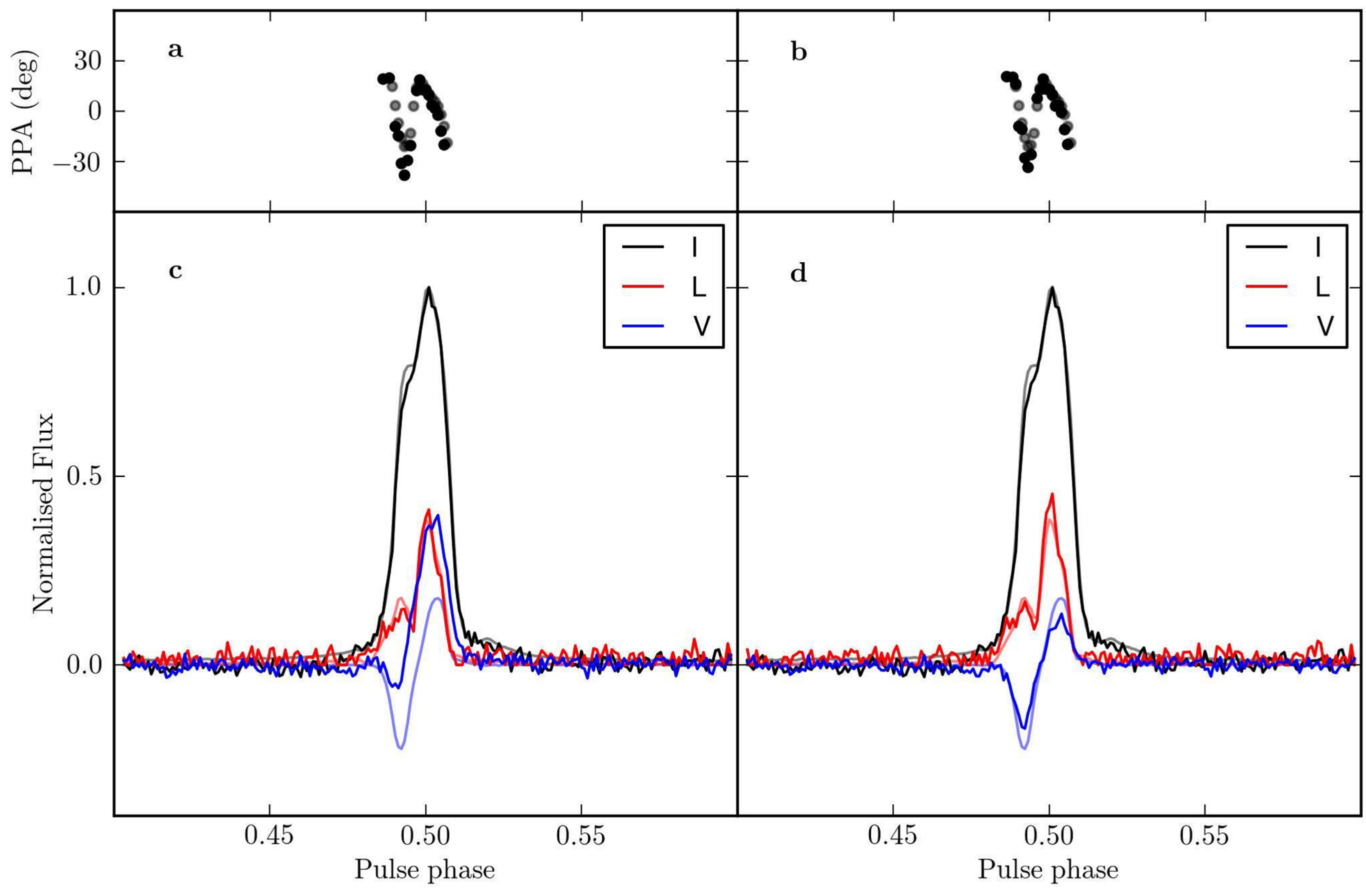

Extended Data Fig. 2 | The polarisation position angle swing (panels a and b) and average polarisation profiles (panels c and d) of PSR J1935+1616. Shown are Stokes I (black), linear polarisation (red) and circular polarisation (blue). For comparison, the pulsar profile and PPA from the literature (at 1.4 GHz[63]) is shown using more transparent colours. (**a**) and (**c**): before applying the leakage calibration discussed in the text and Faraday-correcting using the true rotation measure[62] of the pulsar (-10.2 rad m^{-2}), that is we are also ignoring the delay between polarisation hands. (**b**) and (**d**): The leakage calibrated data, Faraday-corrected using the RM determined using the PSRCHIVE tool rmfit, which, in essence, accounts for the delay between the polarisation hands. This illustrates the polarisation calibration used for the SGR 1935+2154 bursts. Note that the absolute value of the PPA has been shifted to visually compare our observations with the literature.